# Free convective controls on sequestration of salts into low-permeability strata: insights from sand tank laboratory experiments and numerical modelling

Vincent E. A. Post · Craig T. Simmons

**Abstract** Using sand tank experiments and numerical models, local-scale solute-transport processes associated with free convection in both the region surrounding as well as within discrete low-permeability strata are explored. Different permeability geometries and contrasts between high- and low-permeability regions are tested. Results show that two free convective processes occur at different spatial and temporal scales. In the high-permeability region, salinisation was rapid and occurred predominantly by free convective flow around the low-permeability blocks (interlayer convection). A free convection flow field also became concurrently established within the low-permeability lenses (intralayer convection). It was found that upward vertical flow created by the large-scale interlayer free-convective flow field in the high-permeability region retards salinisation of the lenses as buoyant freshwater displacements oppose the downward penetration of dissolved salts. Salinisation of the low-permeability structures eventually takes place from below as saltwater is dragged upwards. This bottom up convective salinisation process of low permeability strata has not been reported in previous literature. These results demonstrate that variable-density sequestration of solutes driven by a source resident above the low-permeability layer is a complicated function of the geometry of the permeability distribution and the permeability contrast between low- and high-permeability regions.

V. E. A. Post (✉)
Faculty of Earth and Life Sciences,
Department of Hydrology and Geo-Environmental Science,
Vrije Universiteit,
De Boelelaan 1085, 1081 HV, Amsterdam, The Netherlands
e-mail: vincent.post@falw.vu.nl
Tel.: +31-20-5987402
Fax: +31-20-5989940

C. T. Simmons
School of Chemistry, Physics and Earth Sciences,
Flinders University,
GPO Box 2100, Adelaide, 5001, SA, Australia

## Introduction

Numerous coastal areas throughout the world experience episodic flooding by seawater. Such events may be regular and anticipated, for example tidal flooding, or catastrophic, as in the case of the 2004 tsunami in southeast Asia, the 2005 hurricane Katrina in New Orleans (USA) and the 2007 typhoon Sidr in Bangladesh. Besides more noticeable effects such as loss of life and infrastructure, flooding potentially leads to deterioration of groundwater quality. When seawater infiltrates into the soil and enters the aquifers, freshwater may become contaminated and water resources are adversely impacted (Illangasekare et al. 2006). In addition, the processes of saline transgression and regression may have a similar effect but over much longer geologic time scales (Kooi et al. 2000; Post and Kooi 2005). Of particular importance in the case of seawater flooding is the unstable density stratification that develops when seawater sits on top of fresh groundwater. This may give rise to the process of free convection during which the more saline water migrates vertically downward under the influence of its high density compared to the underlying freshwater. Typically, plumes of saltwater form during this process which can sink down into the aquifer at considerable rates (Simmons 2005; Simmons et al. 2001). Depending on the permeability of the subsurface and the duration of the flood, extensive aquifer salinisation potentially occurs through this free convective process. Free convection processes are equally important in other hydrogeologic phenomena including reflux from salt lakes and saline disposal basins (Simmons et al. 1999; Nield et al. 2008), groundwater contamination (Schincariol and

Schwartz 1990; Liu and Dane 1996) and carbon sequestration (Riaz et al. 2006).

The process of free convection has been extensively studied in laboratory experiments and mathematical analyses. Studies have focused on the stability of the boundary layer (Wooding 1962; Elder 1968; Schincariol et al. 1994; Wooding et al. 1997a) and the growth rate (Wooding 1969; Wooding et al. 1997b) and coalescence of plumes (Bachmat and Elrick 1970; Wooding et al. 1997b). A large body of work exists on the treatment of free convection in homogeneous porous media but the question of free convection in heterogeneous porous media is still an area that warrants exploration. Studies by authors such as Simmons et al. (2001) and Prasad and Simmons (2003) reported on the results of free convection numerical experiments in which a stochastic permeability field was used to represent the heterogeneity. Results showed that increased heterogeneity tended to increase instability at earlier times but at the same time promoted stability at later times due to increased mixing between the saline and freshwater plumes. Prasad and Simmons (2003) also found that increasing the presence of horizontal low-permeability structures decreased upward and downward vertical fluid flow and thus reduced the degree of instability. In numerical experiments by Simmons et al. (2001), growth conditions in vertical high-permeability zones were enhanced because adjacent vertical low-permeability structures limited horizontal-dispersive mixing. These results clearly showed that the geometry of the heterogeneous permeability fields is a critical factor in the onset, growth and decay of free convective flow. A recent comprehensive discussion on the matter of free convection in heterogeneous porous media is presented by Nield and Simmons (2007). This discussion highlights numerous issues including the ongoing debate over the applicability of the traditional Rayleigh number (the dimensionless number used for predicting the onset of free convection) in heterogeneous systems.

Natural porous media always contain at least some degree of permeability stratification and hence the free convection process will be affected by this heterogeneity. Sedimentary layering is typically horizontal. Fracturing can occur in any direction. Vertical structures are created by bioturbation (digging, root channels), cracking by desiccation or ploughing underneath agricultural soils. This creates alternations of varying complexity of low- and high-permeability structures over a wide range of length scales. To date, few studies have been published that focus specifically on the effect of such structures on the free convection process. Recently, Simmons et al. (2008) considered the modes of free convection in a fractured low-permeability layer and showed that the inclusion of explicit discrete fractures were critical in controlling the onset conditions for free convection. Other studies on the effects of realistic heterogeneous structures (Schincariol et al. 1997; Simmons et al. 2001) have generally looked at macroscopic processes and indicators (e.g., salt fluxes, extent of fingering) in more complex heterogeneous fields. These analyses have been conducted at the scale of the overall heterogeneous porous layer without a direct interrogation of the physical solute transport processes occurring at much more local scales within the highly heterogeneous permeability distribution, i.e., by zooming in to more carefully examine the transient processes occurring both within and surrounding a low-permeability lens, for example, to examine the precise effect that the low-permeability layer or lens has on free convection. It is expected that the presence of low-permeability zones retards the free convection process as they preclude the vertical migration of saline and freshwater plumes. Salinisation of the low-permeability zones themselves is expected to occur at a different rate than in the high-permeability zone and may be controlled by both free convection and/or diffusion, depending upon the permeability of the low-permeability layer. Indeed, the salinisation process may occur exclusively through very slow diffusion of dissolved salts if the permeability of the layer becomes very low. The importance of the presence of low-permeability structures further resides in the fact that once salinised they constitute a source of salt once the high-permeability sediments have been flushed following the flooding event (Volker and Van der Molen 1991; Eggenkamp et al. 1994; Groen et al. 2000).

The precise solute transport processes that lead to salinisation of low-permeability layers in the presence of free convective phenomena have not previously been explored. It is not clear to what extent and under what precise hydrogeologic conditions the solute transport processes are controlled by diffusion and/or free convection. An understanding of these processes is important as they influence the length and time scales associated with salinisation. The objective of the present study is to establish how structured low-permeability distributions affect the dynamics of convective-flow for characteristic natural geologic systems and the salinisation (sequestration) of the low-permeability layers. Critical questions arise: What are the solute transport processes that occur at the local scale both within and surrounding the low-permeability lens? What are the processes that lead to the salinisation of the low-permeability layer? To what extent are the salinisation processes controlled by diffusive versus free convective transport, in a system which is clearly controlled by free convective flow associated with a fluid density inversion? How are the low-permeability layer salt sequestration processes affected by key hydrogeologic properties? What role does the permeability configuration and its geometry play? An attempt has been made to explore answers to these questions using laboratory experiments conducted in a sand tank (with heterogeneity length scale on the order of decimeters) and variable-density groundwater flow and solute transport modelling. The intention is not to develop a universal theory but rather to develop an initial understanding of the precise salinisation mechanisms in these heterogeneous systems using specific demonstration examples.

## Materials and methods

The study consisted of a laboratory sand tank experiment which is also simulated using a numerical model. Additional numerical model simulations were then conducted in order to generalise the findings of the laboratory experiment to a range of other permeability configurations. The comparison of the laboratory experiment with numerical modelling provides a more confident foundation upon which to generalise the results through additional numerical simulations.

### Tank experiment

The laboratory tank consists of two parallel glass plates that measure 110 cm in length and 60 cm in height which is filled with sand. The two plates have an internal separation of 5 cm. Plastic taps located at 5 cm intervals on both sides of the tank allowed flushing and draining. Sand was prevented from entering the taps by means of nylon cloth lining inside the tank. Saline water was introduced to the sand by means of a rectangular source box sitting on top of the sand. The walls of the box were made of PVC and its bottom was a perforated, galvanized iron screen. By maintaining a thin (1–2 mm) layer of

saltwater within the source box a uniform delivery of saltwater to the tank was enforced. Because the experiment focused on free convection, care was taken to avoid any flow driven by hydraulic gradients. To satisfy this aim, the tank was filled with sand to just below the opening of the top tap. This prevented ponding of water above the sand as the top taps allowed water to freely drain from the tank. Moreover, a fixed water level was maintained inside the source box at the same elevation as the opening of the taps. This was done to prevent horizontal flow along the top of the sand. Nevertheless, some horizontal spreading of saltwater from the source box was observed in the experiment.

The tank was packed in such a way as to have a low-permeability rectangular structure inside a more permeable body. The conceptual model for the sand tank experiment and its packing are shown in Fig. 1a. Values for the relevant hydraulic parameters are listed in Table 1. The low-permeability rectangular zone has horizontal and vertical dimensions 48 cm × 10 cm, respectively and its centre is located at 31 and 34 cm from left and bottom of the tank, respectively. The high-permeability material consisted of quartz sand with 84% of the grains having particle sizes in the range 0.5–1 mm. Porosity and hydraulic conductivity of the high-permeability material
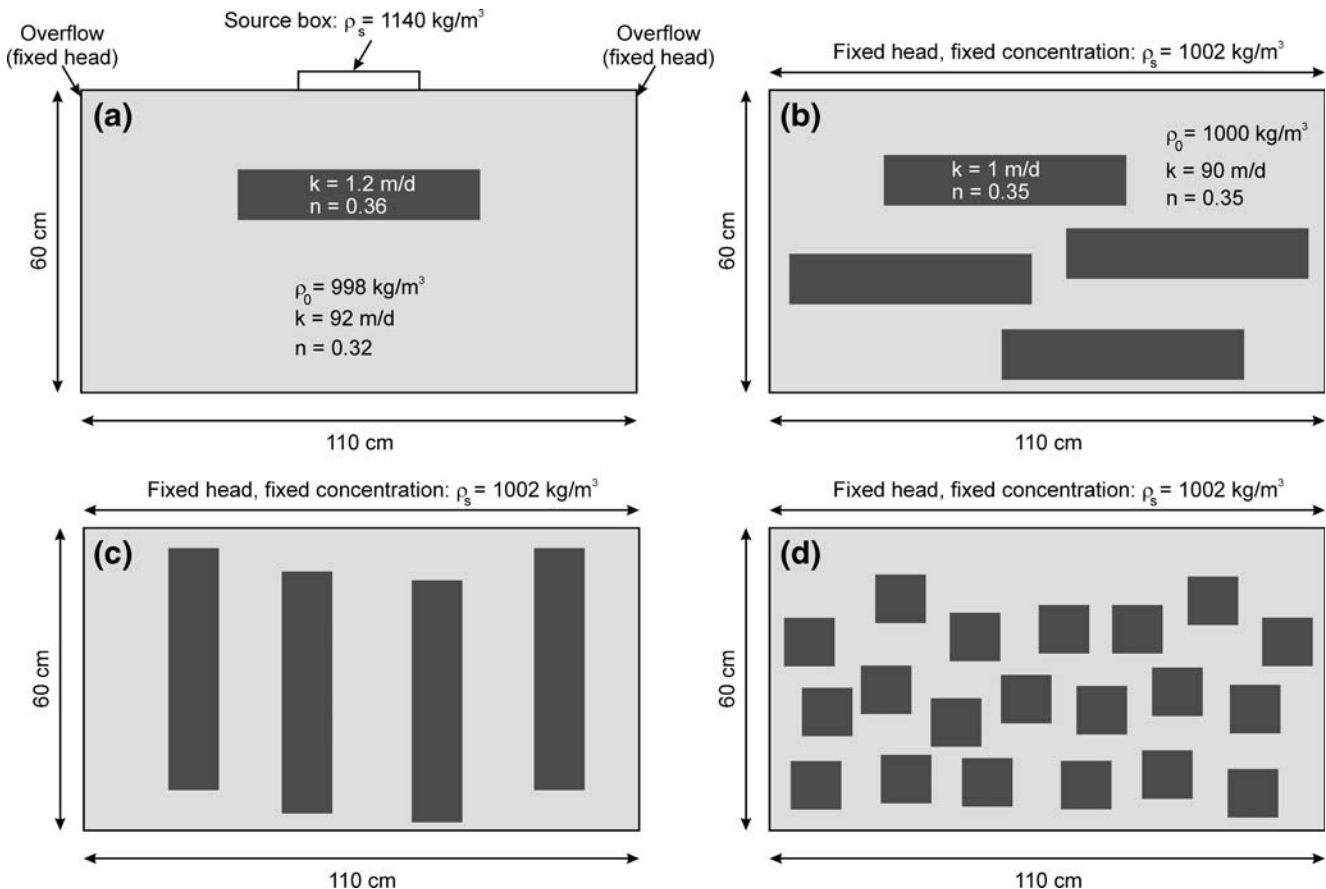


**Fig. 1** Schematic diagrams of the **a** laboratory tank and **b–d** numerical model simulations set ups. **b**, **c** and **d** show permeability configurations *H*, *V* and *B*, respectively. *Dark grey colours* represent low-permeability lenses, *light-grey colours* represent high-permeability regions

**Table 1** Parameter values in the tank experiment and numerical simulations. The diffusion coefficient (D) and dynamic viscosity ($\mu$) values were not quantified for the laboratory tank experiment

| Parameter | Symbol | Value | | Units |
|---|---|---|---|---|
| | | Tank | Numerical model | |
| Density of freshwater | $\rho_0$ | 998 | 1,000 | kg/m$^3$ |
| Density contrast | $\Delta\rho_0$ | 142 | 2 | kg/m$^3$ |
| Molecular diffusion coefficient | $D$ | N/A | 1 10$^{-9}$ | m$^2$/s |
| Freshwater hydraulic conductivity in high-permeability region | $K_h$ | 92 | 180 | m/d |
| Freshwater hydraulic conductivity in low-permeability region | $K_l$ | 1.2 | 1 | m/d |
| Porosity in high/low-permeability region | $n$ | 0.32/0.36 | 0.35/0.35 | Dimensionless |
| Dynamic viscosity | $\mu$ | N/A | 1 10$^{-3}$ | kg/m/s |

were determined from a constant head test in a Darcy tube and were found to be 32% and 92 m/d, respectively. The low-permeability material consisted of glass beads with a grain diameter less that 20 μm. Porosity and hydraulic conductivity of the low-permeability material were found to be 36% and 1.2 m/d respectively.

The tank was packed from the bottom up by mixing sand in a layer of water to avoid air entrapment. Ordinary tap water with a density of 998 kg/m$^3$ was used for this purpose. The saline solution that was introduced at the top of the tank was a 1.9 M CaCl$_2$ (166 g CaCl$_2$ per litre) solution with a density of 1140 kg/m$^3$. CaCl$_2$ was preferred over NaCl to avoid cation exchange reactions between the water and the sediment. Geochemical calculations indicate that the tap water and saline water, as well as mixtures thereof, are undersaturated with respect to calcite. The quartz sand and glass beads contained no calcite. For these reasons, carbonate reactions like calcite precipitation or dissolution are not expected. Subsequent tank experiments employed lower density contrasts but are not shown here because air entrapment (caused by flushing of the tank after the previous experiment) caused noticeable wall effects and are thus not considered to be accurate.

The saline solution was marked with the fluorescent dye fluorescein to allow visual monitoring of the salt plumes. This dye was selected from a number of dyes after ensuring that it was not retarded through sorption compared to chloride in a Darcy tube column breakthrough test. The diffusion coefficients of fluorescein and CaCl$_2$-salt are different (Yamaguchi et al. 1997) but due to the dominance of advective transport and the limited duration of the experiment, these differences in diffusion coefficients are considered negligible. Time lapse photography was used to monitor the progress of the experiment using a KODAK DC290 digital camera. The experiment ran for 7 h and 8 min. Photographs were taken every 2 min during the first 4 h and every 4 min during the last 3 h of the experiment. No image-processing was performed to determine solute concentration distributions. Dispersive effects during the experiment were very small and spatial and temporal salinity variations associated with fingering were easily-discernable visually. The complex patterns that evolved in the experiment were very detailed and did not lend themselves easily to the quantification of concentration distributions. For the purposes of examining the flow and transport processes that occurred, the stained plumes were easily discernible in the time lapse photography. This approach allowed for comparison of the broad spatial and temporal processes in the laboratory and numerical modelling approaches.

## Numerical simulations

Numerical experiments using the variable-density flow simulator SEAWAT-2000 (Langevin and Guo 2006) were set up to generalise the findings using lens permeability scenarios which could more easily be tested within a numerical framework.

The following equations for fluid and solutes were solved:

$$\frac{\partial (n\rho)}{\partial t} + \nabla \cdot \left( \rho \vec{q} \right) = 0 \qquad (1)$$

$$\frac{\partial (nC)}{\partial t} = \nabla \cdot (nD \cdot \nabla C) - \nabla \cdot \left( \vec{q} C \right) \qquad (2)$$

where $n$ is the porosity (dimensionless), $\rho$ is the fluid density (M/L$^3$), $\vec{q}$ is the Darcy velocity (L/T), $C$ is the solute concentration (M/L) and $D$ is the dispersion tensor (L$^2$/T). For a fluid of variable density the Darcy velocity is expressed as:

$$\vec{q} = -\frac{k}{\mu} \left( \nabla P + \rho \vec{g} \right) \qquad (3)$$

where $k$ is the intrinsic permeability tensor (L$^2$), $\mu$ is the dynamic viscosity (M/L/T), $P$ is the fluid pressure (Pa) and $\vec{q}$ is the gravitational acceleration vector (L/T$^2$). Within SEAWAT-2000 the governing equations are rewritten in terms of equivalent freshwater head (Langevin and Guo 2006) such that they can be solved using the standard MODFLOW-2000 code. A linear equation of state is used to relate solute concentration to density.

It was considered important as a first step in the exploration of these phenomena to numerically simulate these processes at the laboratory scale rather than at a larger field-scale setting. Field-scale numerical simulations would increase computational complexity further and in

the absence of any available data to test the relevant processes and physics, would not provide any means of assessing model reliability. The model domain had the same dimensions as the laboratory tank, i.e., 110 × 60 cm (Fig. 1). According to the discretisation criteria for free convection simulations of Kooi et al. (2000), the cell size required to resolve the diffusive boundary layer and the fingers emanating from it must satisfy the criteria:

$$\Delta z < \left( \frac{Ra_{cr}\mu nD}{\Delta \rho g k} = \frac{7 \times 1 \times 10^{-3} \times 0.32 \times 1 \times 10^{-9}}{142 \times 9.81 \times 1.1 \times 10^{-10}} = 1.5 \cdot 10^{-5} m \right)$$
(4a)

$$\Delta x < \left( 2\Delta z = 3.0 \cdot 10^{-5} m \right)$$
(4b)

where $\Delta z$ and $\Delta x$ are the cell height and length, respectively, and $Ra_{cr}$ is the critical Rayleigh number, which is the value of the Rayleigh number above which convection will occur. Note that, following Kooi et al. (2000), a value of 7 is used here for the critical boundary layer Rayleigh number $Ra_{cr}$ instead of the macroscopic layer Rayleigh number $Ra_{cr}=4\pi^2$, the latter which applies to the classic Horton-Rogers-Lapwood problem. The motivation is that the value of $Ra_{cr}=7$ applies to free convection development in a local boundary layer (Wooding et al. 1997a) whereas the critical value for the Horton-Rogers-Lapwood problem represents a macroscopic measure of stability. From Eqs. (4a) and (4b) it follows that using exactly the same parameters in the numerical simulations as in the laboratory experiment would require a number of cells that is impossible from a computational point of view. Instead, a coarser grid was used that was designed according to the steps outlined below. The objective of this simulation was to compare the general qualitative characteristics of convective behaviour between the laboratory experiment and the numerical simulation.

The numerical simulation of the tank experiment had the same permeability distribution as shown in Fig. 1a. The hydraulic conductivity of the low-permeability lens was fixed at 1.2 m/d (Table 1). The hydraulic conductivity of the high-permeability sand was varied to achieve a more satisfactory match between laboratory results and the numerical simulation. This was because during preliminary model runs it was found that this value had to be adjusted to obtain better agreement between the rate of downward descent of the plumes. The final value used in the numerical simulation was two times higher than the value measured in the column experiment, i.e., 180 m/d. This approach is justified since a difference of a factor of 2 is well within the range of uncertainty that is typical for this parameter (Simmons et al. 2002). It should be noted here that a small Darcy column was used to measure the hydraulic conductivity of the high-permeability material. Measurements were not made in-situ at the scale of the tank because it was packed with both high-permeability and low-permeability media in place. Previous studies have shown that scale differences and the "wall effect" can increase the hydraulic conductivity within the tank

when compared with that determined using other methods. Simmons et al. (2002) found that the hydraulic conductivity of the high-permeability medium used in their experiments was about three times higher when measured in-situ within the tank than when compared to that obtained using a smaller Darcy tube. Simmons et al. (2002) noted that the packing of a porous medium close to a smooth wall is altered by the presence of the wall and that the effective permeability of a thin layer whose thickness is of the order of particle dimensions, may have permeability that is increased by up to about twice that of the main body of the medium. The observation of coloured dye movement close to the glass surface may be sensitive to this effect.

A fixed head was assigned to the boundary along the top of the model domain. This means that inflow and outflow was simulated along the entire upper boundary, which is in accordance with the conditions that existed during the laboratory experiment. The concentration at the top model boundary was fixed at the location of the source box. The left, right and bottom boundaries were closed for flow and solute. All cells outside the source box were assigned an initial concentration corresponding to freshwater at the start of the simulation. Fingering was triggered by adding noise (representing very small local scale heterogeneity and perturbations to flow in the vicinity of the boundary layer) to the fixed concentrations representing the source box because early numerical results suggested that only two outer-edge lobes were generated in the case where additional noise was not added to the fixed concentrations representing the source box. Due to the dominance of free convective processes noted during the tank experiment, mechanical dispersion was considered negligible. A uniform diffusion coefficient of $10^{-9}$ m/s was assigned to all model cells.

In addition to the numerical simulation of the actual sand tank experiment, a larger number of numerical simulations were performed to test the effect of different permeability distributions. In these simulations, a smaller density contrast of $\Delta \rho = 2.0$ kg/m$^3$ between the saline and freshwater was used. For the purpose of these simulations it was considered advantageous to use a lower density contrast since it slows down the rate of plume descent. This is important because it increased the duration of the simulation which in turn increased the opportunity for salt sequestration into the low-permeability zones, especially in those experiments in which solute transport within these lenses was dominated by diffusion. Results (shown later) also reveal that this much lower density contrast still leads to free convection driven by density differences in the high-permeability region which is a critical requirement for these analyses. That is, this lower density contrast still creates free convective flows in the sand tank whilst at the same time substantially slowing down plume development and hence maximising sequestration opportunity. Whilst these modelling choices clearly lead to enhanced sequestration, results (shown later) reveal that sequestration into the low-permeability lens also occurred in the sand tank experiments for the much higher density

contrast. However, in the laboratory experiment, it was clearly advantageous and somewhat necessary to use a higher density contrast to maximise the effect of density driven free convection so as to substantially reduce laboratory experimental runtimes. With a lower density contrast used in the subsequent numerical simulations used to generalise findings, it was now possible to use a grid that satisfied Eqs. (4a) and (4b) which is advantageous where they can be feasibly employed from a computational point of view. It follows from Eqs. (4a) and (4b) that the maximum cell dimensions are $\Delta x$=2.4 and $\Delta z$=1.2 mm. Consequently, the grid had 468 columns in the horizontal and 510 rows in the vertical direction. Even though this is a relatively small number of cells, runtimes for individual simulations reached up to 120 h on the national computing cluster of the Netherlands (SARA). These runtimes posed a practical limitation to the number of model runs that could be performed, as well as to the possibility for grid refinement.

All boundaries are closed for both flow and solute transport except for the top of the model domain, which is a fixed head, fixed concentration boundary that represents a salt source. Both numerical model and experimental solutions are controlled by the location and type of boundary conditions that are used. In this case no flow boundaries are used on the vertical and bottom boundaries of the tank experiment and simulations. One may think of each of these no flow boundary conditions loosely as a symmetry axis, if one assumes that the same permeability configuration is reflected at both sides of the tank. In reality, these are the most convenient form of boundary condition for the laboratory experiment and as such they have also been used in the numerical simulations. Importantly, more complex boundary conditions are not warranted nor justified in this initial investigation since there is no physical basis (e.g., field observations) upon which to justify a more complex formulation of the boundary conditions. Further work could explore the nature of the boundary conditions employed and how they affect the flow field solutions.

Since increasing the number of cells was not possible without resulting in unacceptably long runtimes and computer memory requirements, the following approach was taken while testing for grid convergence. Convergence tests were performed for simulations with a density contrast of $\Delta\rho$=1.0 kg/m$^3$. Halving $\Delta\rho$ while holding all other parameters constant, means that the required cell dimensions become twice as high (Eqs. 4a and 4b) and it was therefore possible to run these simulations using a grid of 234 columns and 255 rows. Comparison of simulations with $\Delta\rho$=1.0 kg/m$^3$ that employed a grid of 234 × 255 columns and rows with the grid of 468 × 510 columns and rows showed that these yielded the same results in terms of the thickness of the diffusive boundary layer, the wavelength of the plumes and the rate of downward descent. Since the physical dimensions of these features scales linearly with the density contrast (Kooi et al. 2000) it was reasoned that if halving the cell size for simulations with a density contrast of $\Delta\rho$=1.0 kg/m$^3$ has

no effect on the outcomes, the same would be true for the simulations with $\Delta\rho$=2.0 kg/m$^3$. It was therefore concluded that the employed grid for the simulations with $\Delta\rho$=2.0 kg/m$^3$ was adequate.

The solute concentrations of all the cells in the model domain were assigned a uniform initial concentration of zero at the start of the simulation. Fingering was triggered by numerical and round-off errors. The total simulation time was 40 d with a variable transport time step size. The maximum time step size that was allowed was 0.01 d, or smaller if required to meet the Courant condition. It should be noted that this simulation time of 40 d is substantially larger than the 7 h of the laboratory experiment owing to the much lower density contrast employed in the numerical modelling analyses.

Three realisations of permeability fields were used that are conceptualised to be representative end-members for field conditions (Fig. 1b–d): horizontal, vertical and "blocky". These will be referred to as configuration H, V and B respectively. Configuration H is considered typical for rocks in which lenses of low-permeability material occur, such as for example in aquifers made up of fluvial deposits containing clay lenses (Herweijer 1997). Configuration V is more typical for geological units that have been cracked or fractured or in which the bedding planes are oriented vertically due to (tectonic) tilting. Configuration B is intermediate between configurations H and V. It is expected that the orientation of the lenses will either impede or promote salinisation as they (1) determine the effective permeability that the salt fingers experience during their downward migration and (2) control the extent of horizontal mixing and plume coalescence (Simmons et al. 2001). The ratio of the horizontal to vertical surface area ($r_{hv}$) of the low-permeability zone in configurations H, V and B is 4.72, 0.22 and 1.04 respectively. The physical significance of these numbers in terms of free convection is that a high value is expected to retard the overall salinisation rate whereas for ratios that are << 1, horizontal mixing is minimised thus preventing finger coalescence. The volume of low- and high-permeability regions was held constant between simulations.

The freshwater hydraulic conductivity of the high-permeability region was $K_h$=90 m/d in all simulations. For each of the configurations H, B and V, eight simulations were performed with different permeability contrasts between the low and the high-permeability zones. This was done by varying the freshwater hydraulic conductivity of the low-permeability region between 45 and 0.01 m/d. The resulting simulations had permeability contrasts of $K_h/K_l$=2, 10, 18, 30, 45, 90, 900 and 9,000, where $K_h$ and $K_l$ are the freshwater hydraulic conductivities of the high- and low-permeability regions, respectively. This resulted in a total of 24 simulations. The permeability contrast is designated by a subscript, e.g., H$_{9000}$ represents the configuration with the horizontally oriented low-permeability structures with a permeability contrast $K_h/K_l$=9,000.

Simulation B$_{9000}$ was run to 30 d only because for a simulation time of 40 d the calculations would not

complete within the wallclock time limit of 120 h on the supercomputing cluster.

Individual simulations were compared by visual inspection of the free convective patterns that developed as well as by computing the total amount of solute present (SP) in the system, which varies as a function of time:

$$SP = \int \int (\rho - \rho_0) dx dz \qquad (5)$$

where $\rho_0$ is the initial density and $x$ and $z$ denote the coordinates in the horizontal and vertical direction,

respectively. The integration was performed at various times over the entire model domain as well as over the high- and low-permeability zones separately. These time dependent quantities will be referred to as SP, $SP_{hi}$ and $SP_{lo}$, respectively.

## Results and discussion

### Tank experiment

Figure 2 shows the plume development in the sand tank with time. Due to local heterogeneities near the source
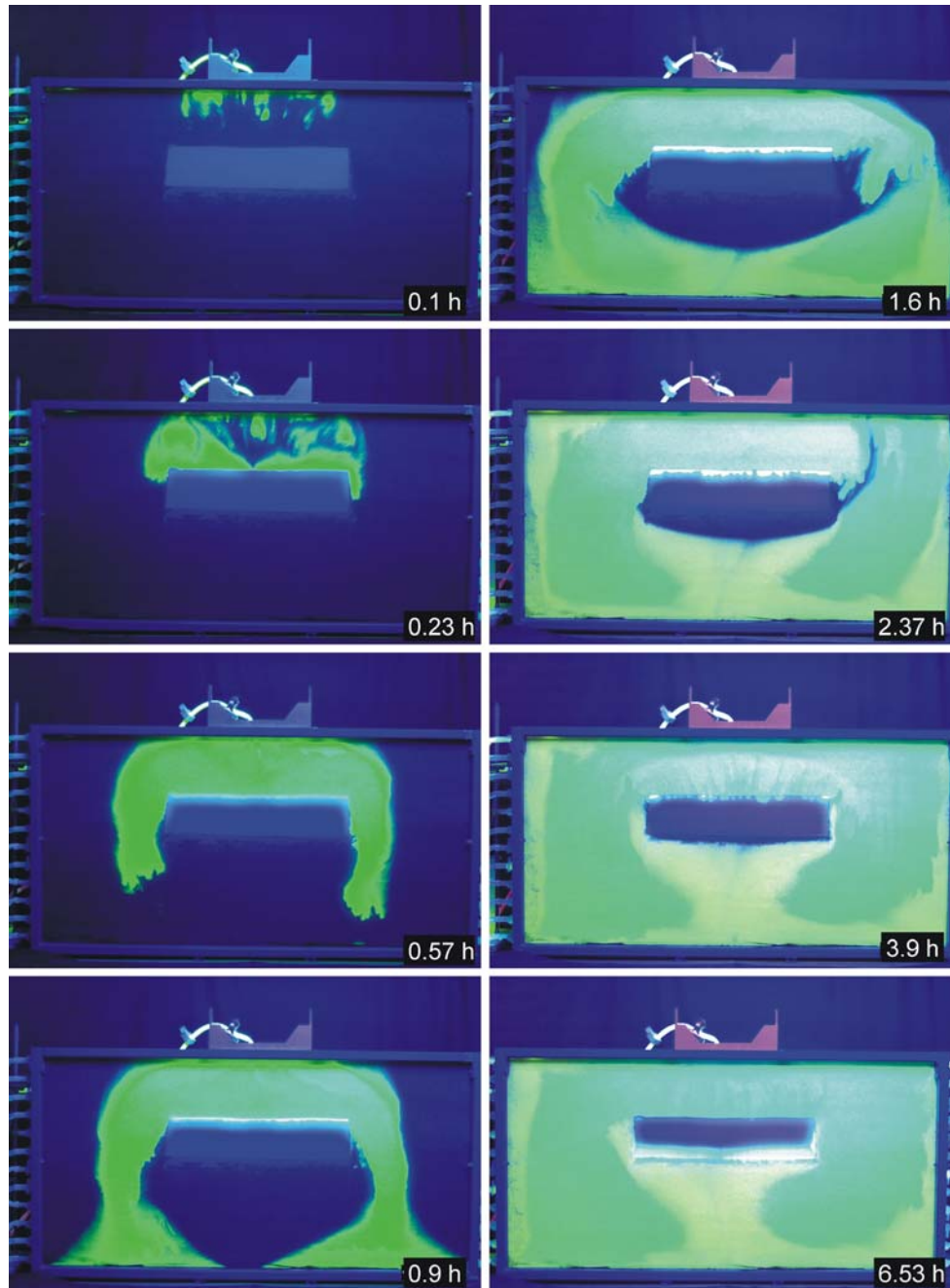


**Fig. 2** The development of salt fingers with time in the laboratory experiment. Snapshots are taken at times 0.1, 0.23, 0.57, 0.9, 1.6, 2.37, 3.9 and 6.53 h after the start of the experiment

box, salt plumes immediately develop as soon as the saline water infiltrates into the porous medium. After approximately 0.17 h, the salt plumes reach the low-permeability structure and horizontal spreading of the saline plume starts. After 0.6 h, descending salt plumes that flow around the low-permeability lens have reached the bottom of the tank. As soon as the salt plumes reach the bottom of the tank, significant horizontal spreading occurs. At the same time, a diffusive boundary layer has developed at the top the low-permeability lens, which is visible as a bright white zone just below the top of the lens (Fig. 2). The development of gravitational salt fingers from this boundary layer starts to be visible after approximately 1.5 h and suggests that free convection is occurring in the low-permeability lens at early times.

The freshwater that resides below the low-permeability lens becomes completely surrounded by saline water. The ongoing supply of saline water from the top boundary and the lateral spreading of dense plume along the bottom of the tank causes the entrapped freshwater lens to move upward. This lens thins and elongates as the low-permeability layer impedes its upward movement. Occasional 'jets' of upwelling freshwater can be seen to divert and escape upwards through the downward moving plumes of saline water, particularly on the right side of the low-permeability zone.

Once the high-permeability material in the tank is almost completely filled with saltwater, the 'jets' become less frequent and lose strength. The only means of upward freshwater movement is through the low-permeability lens, which becomes apparent from the disappearance of the salt plumes within this structure. The fingers that have formed are pushed upward and they completely disappear by the end of the experiment. Freshwater fingers move upwards across the top of the low-permeability layer (Fig. 2) but they rapidly mix with saltwater in the high-permeability zone. Surprisingly, salinisation of the low-permeability lens after approximately 4 h is predominantly from below the low-permeability layer as the positive buoyancy of the freshwater creates an upward directed flow field in which the saltwater is dragged upwards from the high-permeability sediments into the base of the low-permeability structure.

## Numerical experiments

The numerical simulation of the sand tank experiment is shown in Fig. 3. A movie which shows the comparison between the laboratory experiment and the numerical simulation is available as Electronic supplementary material. The general spatial and temporal characteristics of salinity patterns produced in the numerical simulation are in very good agreement with those observed in the laboratory tank experiment. These include the initial vertical downward movement followed by horizontal spreading as the plumes hit the low-permeability lens,

the entrapment of freshwater below the lens, the jets of freshwater that escape through the sinking salt plumes, the 'pushing back' of salt that has entered the low-permeability lens from above and the entrainment of saline water into the lens from below. In a strict quantitative sense, there are still some small differences between the results of the laboratory experiment and the numerical model. A small difference is observed in the speed of descent of the plumes in the high-permeability medium. The dense plumes reach the bottom of the sand tank slightly earlier in the numerical simulation than in the laboratory experiment. During later experimental times, the displacement of freshwater from the tank by saltwater that enters from above appears to be somewhat slower in the numerical model compared to the tank experiment. Furthermore, the development of the diffusive boundary layer and subsequent fingering into the top of the low-permeability lens occurs earlier in the laboratory experiment than in the numerical simulation. Further refinement of the agreement between the numerical simulations and the laboratory experiment could have been made through image analysis of the photographs of the tank experiment to resolve quantitative concentration patterns as well as a more rigorous calibration process. This may have included further variation to the hydraulic conductivity of the high-permeability medium, and possibly some variation to the hydraulic conductivity of the low-permeability medium which were not tested. Unfortunately, the run time for each simulation was so restrictive that it was not considered feasible to aim for a perfect calibration here. The very good agreement obtained was satisfactory. In particular, the ability of the numerical model to match the general spatial and temporal characteristics of the laboratory experiment demonstrates that a confident platform was found upon which to base the generalised set of numerical models that employ different heterogeneity.

Figure 4 shows the development of the solute concentration pattern and the flow vectors for simulation $H_{90}$. Initially, a diffusive boundary develops from which salt plumes emanate after 0.6 d and move downward into the aquifer. After 1.5 d, the plumes in the central part of the domain reach the top of the uppermost low-permeability lens and further downward migration is hampered. Consequently, horizontal migration of the salt plumes starts to occur as well as diffusive salinisation of the lens. On both sides of the uppermost lens salt plumes continue to sink down unhindered until they reach the top of the lower lenses. Here the salt plumes are diverted towards the left- and right model boundaries and then sink down further. Spreading of the salt mass towards the centre of the model domain is prevented by the freshwater that is moving upwards as well as sideways.

The salt plumes reach the bottom of the model domain after 6.7 d. By that time, a fairly constant flow pattern has been established in which saltwater essentially flows
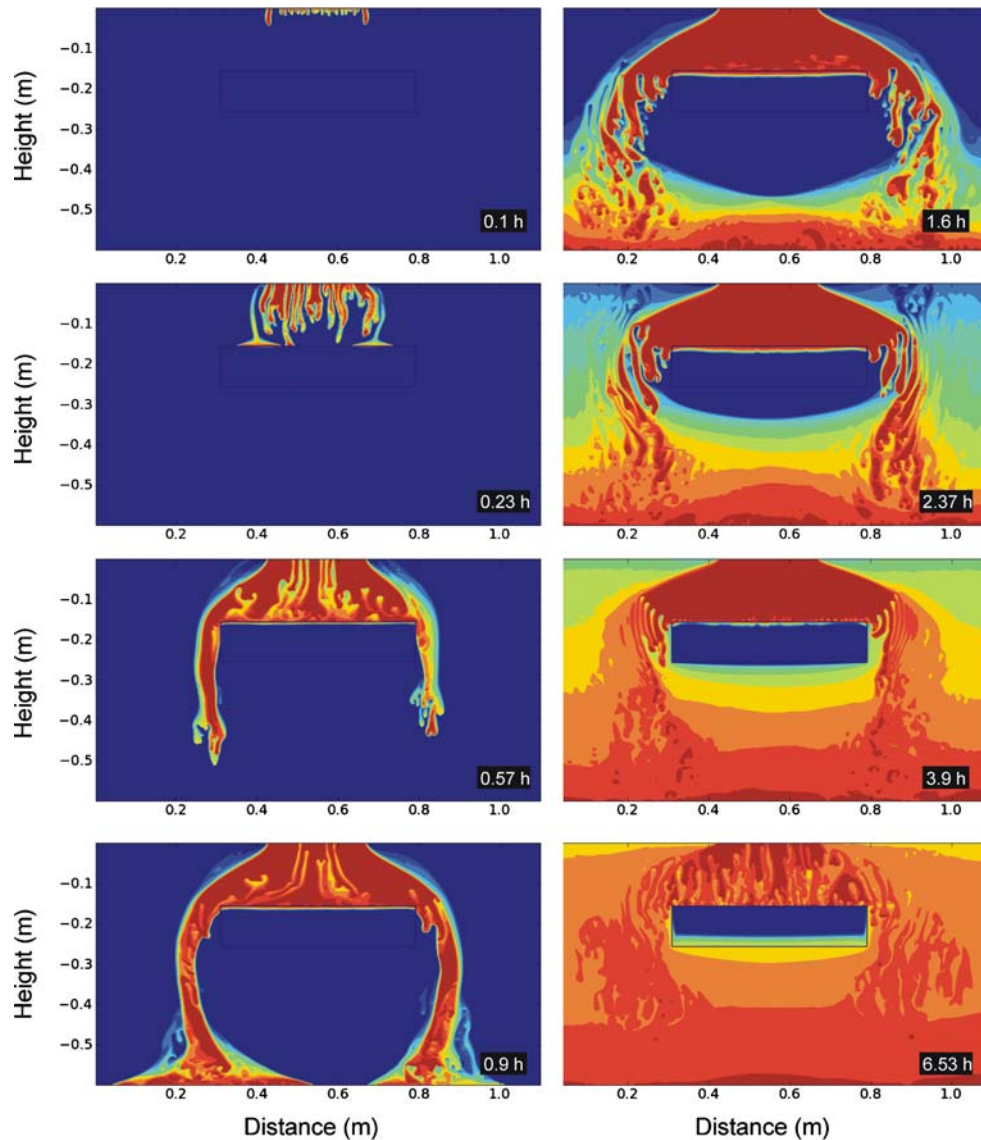
**Fig. 3** The development of salt fingers with time in numerical simulation of the laboratory experiment. Snapshots show the salinity distribution after 0.1, 0.23, 0.57, 0.9, 1.6, 2.37, 3.9 and 6.53 h since the start of the experiment

downward near the left- and, to a lesser extent, right-hand boundaries and freshwater moves upward in the central part of the model domain. Particularly strong vertical upward flow occurs in the high-permeability part of the model domain, immediately adjacent to the vertical sides of the low-permeability lenses. Jets of freshwater can be seen to escape upwards on a regular basis. After approximately 20 d, when concentration gradients in the high-permeability part of the model domain become much smaller, the convective flow cell becomes weaker. Ultimately, as density gradients dissipate, diffusion becomes the dominant transport mechanism. Flow eventually ceases altogether upon complete salinisation of the system.

The larger scale, interlayer free convection pattern (defined as density driven flow that occurs outside the low-permeability layers) also drives intralayer flow

(defined as density driven flow that occurs within the low-permeability layers) as is seen by the development of upward flow components inside them. This is illustrated in more detail in Fig. 5, which shows the flow vectors at different times in the low-permeability lenses. Initially, the vertical flow components are very small. Some downward flow occurs where the plumes hit the low-permeability lens after approximately 2 d. After 3 d, a zone of upward flow starts to develop in the top lens, which continues to grow with time and has been fully established after 4 d. A similar pattern of flow vectors develops in the other three lenses during later times. The magnitude of the vertical flow components appears to be related to the amount of freshwater trapped below and inside the lenses. This magnitude has clearly decreased after 30 d in the two lowermost lenses after their salt mass has increased. Upward flow
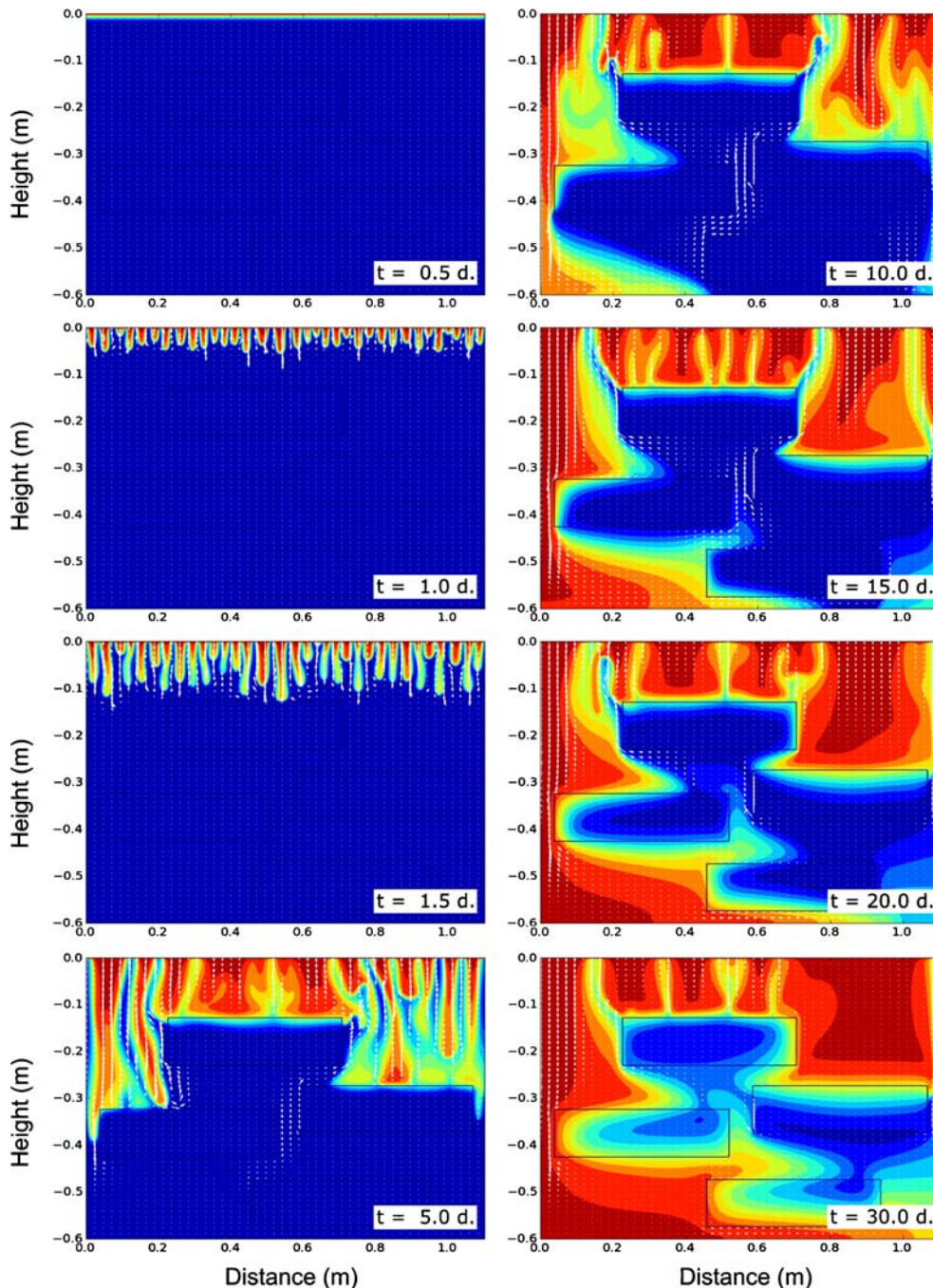
**Fig. 4** The development of salt fingers and flow vectors with time for simulation H$_{90}$. Results are shown for 0.5, 1.0, 1.5, 5, 10, 15, 20 and 30 d since the beginning of the simulation. Only the vector in every tenth column or layer is drawn

inside the uppermost lens and the associated dragging up of saltwater remains an important process, however, due to the buoyancy of the entrapped freshwater.

Despite the differences in lens configuration and density contrast between the saline and freshwater, the qualitative flow and transport features that were observed in the laboratory experiment are also clearly recognised in the numerical simulations. Fingering in the lenses is not as apparent in the model simulations as in the laboratory experiment due to the lower density contrast that was used.

The effect of intralayer convection on the SP$_{lo}$ is clearly visible in Fig. 6 (solid black line): Salt does not enter the low-permeability lenses until after 2 d (Fig. 6g). Salt then starts to accumulate almost linearly with time. After 4 d, the rate of salinisation starts to decrease markedly, which can be attributed to the intralayer vertical flow components that slow down salinisation through the top horizontal faces of the lenses. After approximately 12 d, the rate of salt accumulation in the low-permeability lenses increase again. Initially this is due to the diffusion of salt from
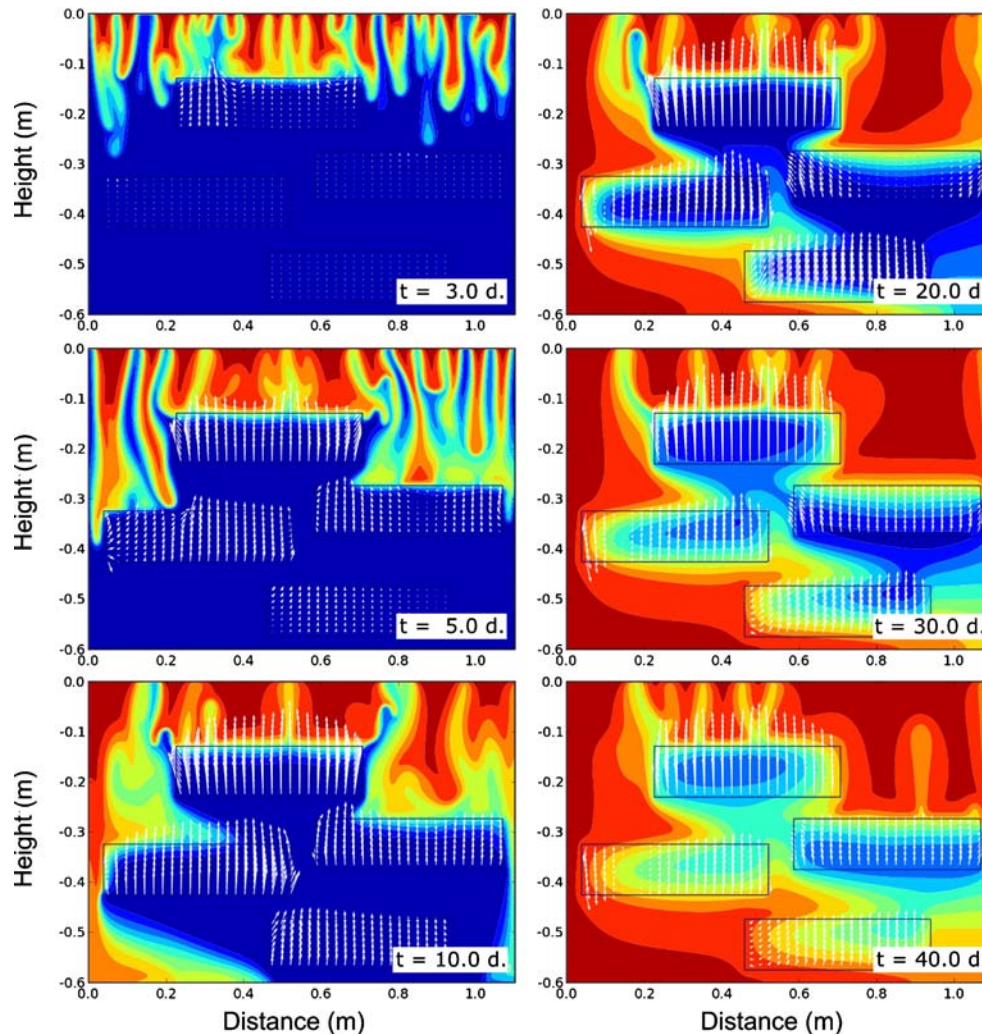
**Fig. 5** The development of salt fingers and flow vectors within the low-permeability lenses with time for simulation $H_{90}$. Results are shown for 3, 5, 10, 20, 30 and 40 d since the beginning of the simulation. The flow vectors have been elongated by a factor of 100 compared with Fig. 4. Only the vector in every tenth column or layer is drawn

above in the rightmost lens in which flow velocities remain very small (cf. Fig. 5). Later on, after approximately 15 d, saltwater that has flowed around and underneath the lenses starts to be dragged into them from below. The $SP_{lo}$ versus time curve becomes steeper as a result (Fig. 6g).

In simulation $V_{90}$, the growth and breakup of the boundary layer is essentially the same as in simulation $H_{90}$ (Fig. 7). Zones of upward and downward flow are closely spaced and the flow field is highly transient during the initial phases of plume descent. Intricate, dynamic salinity patterns occur around the upper corners of these structures where upward migrating freshwater plumes 'compete' with downward sinking saline plumes. The upward flow of freshwater plumes seems to be mainly localised immediately along the boundaries of the low-permeability structures. For this reason, very little salt enters the low-permeability lenses until 8 d after the start of the simulation. It is not until the high-permeability region of the model

domain becomes almost completely saline that the salt mass within the low-permeability zones starts to increase. This is clearly visible in the curves of $SP_{lo}$ versus time (Fig. 6h) which shows only a moderate increase during the first 8 d of the simulation. $SP_{hi}$ on the other hand, increase almost linearly with time during the same period (Fig. 6e). After 8 d, $SP_{lo}$ starts to increase markedly. The mechanism of salinisation initially is predominantly by dragging up of saline water through their lower faces due to the upward flow components that have been established (cf. Fig. 7). Diffusion through the vertical sides of the structures also provides an important contribution to the solute mass in the low-permeability lenses during later stages of the simulation. This process, however, does not gain importance until all freshwater that still resides around the low-permeability structures disappeared from the high-permeability region in the model domain.

For configuration V, SP increases almost linearly with time during the first 10 d of the simulation. The limited
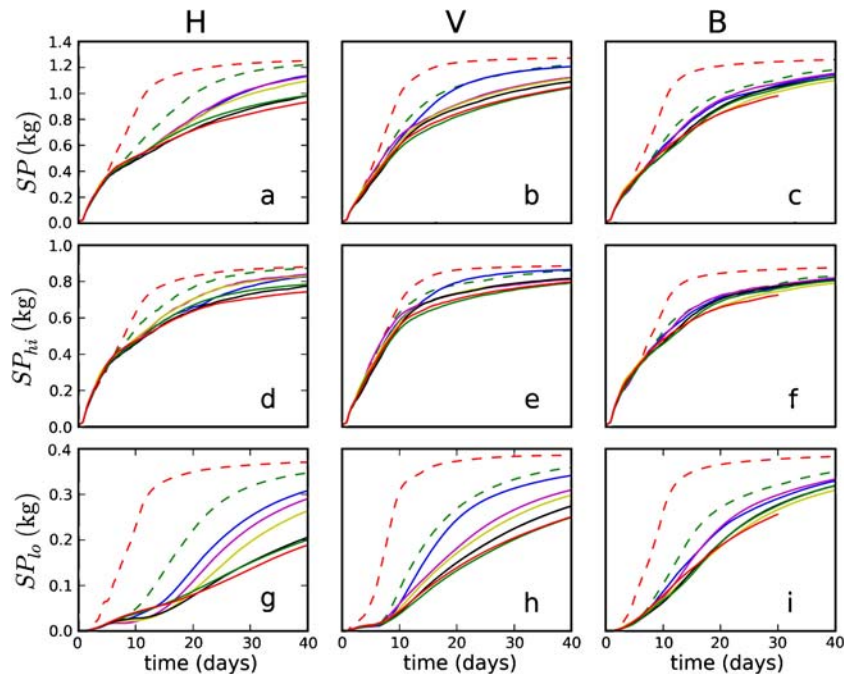
**Fig. 6** The change of *SP* with time for all simulations. Configurations *H*, *V* and *B* are represented in the *left, middle and right panels*, respectively. The *top row* shows the *SP* for the entire domain, the *middle row* the *SP* for the high-permeability region and the *bottom row* the *SP* for the low-permeability lenses. Legend: *Red dashed line*: $K_h/K_l=2$, *green dashed line*: $K_h/K_l=10$, *blue solid line*: $K_h/K_l=18$, *magenta solid line*: $K_h/K_l=30$, *yellow solid line*: $K_h/K_l=45$, *black solid line*: $K_h/K_l=90$, *red solid line*: $K_h/K_l=900$, *green solid line*: $K_h/K_l=9,000$

horizontal spreading thus seems to promote rapid salinisation and as a result SP and $SP_{hi}$ of all simulations of configuration V is significantly higher than for configurations H and B. After 15 d, salinisation rates drop markedly as the driving forces in the high-permeability zone disappear and the rate of salt accumulation within the entire model domain becomes limited by the rate of salinisation of the low-permeability structures.

In the irregular permeability distribution of simulation $B_{90}$, no clear entrapment of freshwater in the high-permeability regions of the model domain is observed (Fig. 8). The saline plumes are diverted around the blocks of low-permeability resulting in an efficient spreading of the salt mass within the system. Consequently, the increase of solute mass within the low-permeability structures proceeds in a very gradual fashion (Fig. 6i). There is no abrupt change in the slope of the $SP_{lo}$ vs. time curve as those that were noticeable in simulations $H_{90}$ and $V_{90}$. The gradual decrease in steepness of the curve with time may reflect the role of the upward vertical flow components, which initially cause impedance of salinisation from above and then subsequently drag salt from below.

The observed control of intralayer flow components on the salinisation of the lenses implies that their permeability is a critical factor in this process. Figure 9e compares $SP_{lo}$ of the three configurations for different permeability ratios after 12 d since the start of the simulation. In general terms, the shape of the curves for the three configurations is comparable but, in contrast to configurations V and B, the data points for configuration H display a minimum for $40<K_h/K_l<100$. This implies that for these permeability contrasts, the retarding effect of the vertical flow components is strongest. As the hydraulic conductivity of the low-permeability regions increases $(1<K_h/K_l<40)$, the descending salt plumes experience increasingly less resistance caused by them during downward plume migration. As a result, the horizontal diversion of the plumes around the low-permeability lens, as visible in Fig. 4, becomes less apparent and eventually disappears as $K_h/K_l$ approaches unity. Consequently, the concurrent interlayer and intralayer convective flow systems that were observed in simulation $H_{90}$, do not have the opportunity to develop as strongly. For much lower permeabilities of the lenses $(K_h/K_l>100)$ the importance of intralayer flow is abated due to the reduction of the flow magnitude within the lenses. This is also reflected by the $SP_{lo}$ versus time curves (Fig. 6g). Simulation $H_{900}$ displays the same shape as the $SP_{lo}$ versus time curve of simulation $H_{90}$, albeit much attenuated. Simulation $H_{9000}$ shows an even more regular increase of $SP_{lo}$ with time (Fig. 6g), suggesting that salinisation is predominantly diffusive. Interestingly, this transitional permeability contrast value of ~100 is equal for all three geometries considered, reflecting the fact that for $K_h/K_l>\sim100$, vertical flow components within the lenses become so weak that solute transport is by diffusion rather than convection.

The permeability of the lenses also affects the rate of salinisation in the high-permeability region of the domain.
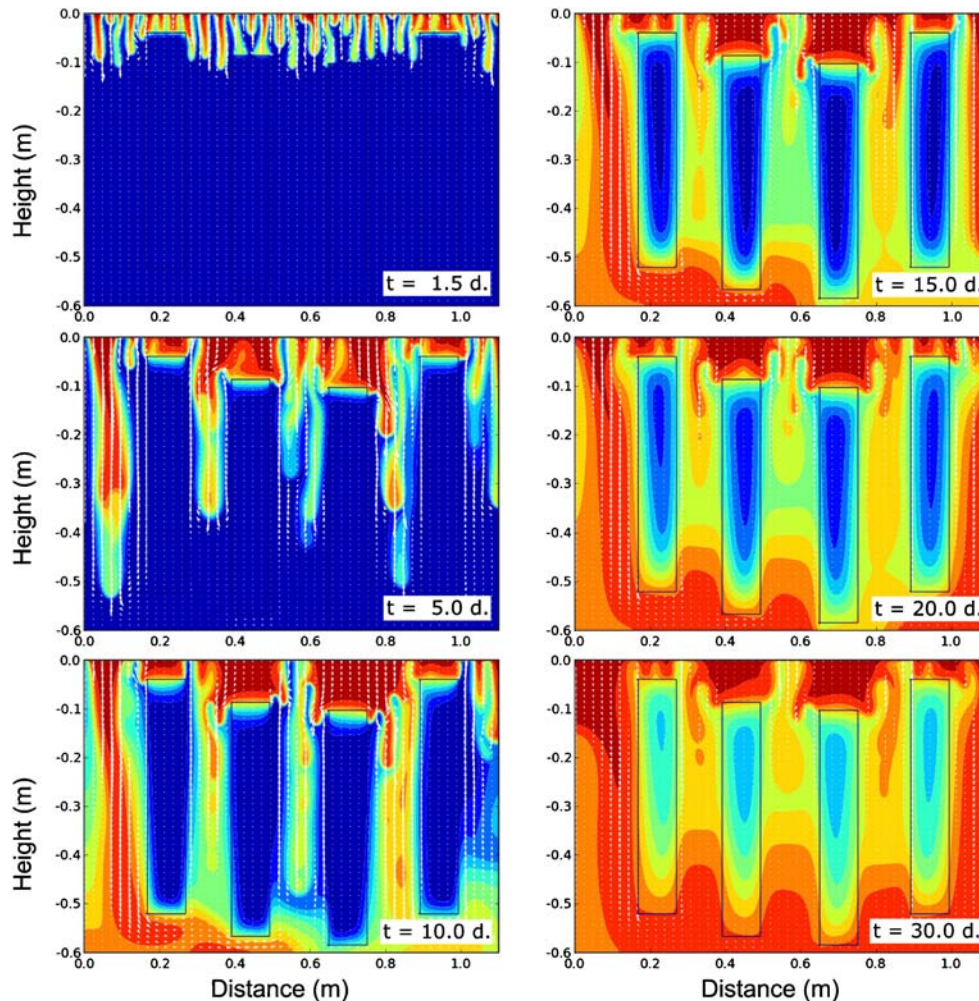
**Fig. 7** The development of salt fingers and flow vectors within the low-permeability lenses with time for simulation $V_{90}$. Results are shown for 1.5, 5, 10, 15, 20 and 30 d since the beginning of the simulation. Only the vector in every tenth column or layer is drawn

This is visible in Fig. 9 (c and d) which shows that the same negative correlation is observed for $SP_{hi}$ and $K_h/K_l$ when $K_h/K_l < 100$ both after 12 and 40 d. This is due to the fact that the density difference that drives convective flow can be maintained for longer when salt is sequestered more rapidly into the lenses.

Besides permeability, lens geometry also determines the importance of the intralayer flow components in relation to the salinisation of the lenses. The intralayer flow field is mainly directed vertically-upward and is thus oriented perpendicular to the horizontal sides of the lens and parallel to the vertical sides. Along the upper horizontal sides, the intralayer flow components work against salinisation of the lens from the outside as they are directed outward from the lens. Along the vertical sides they promote salinisation by moving solutes away from the contact surface between the lens and the high-permeability region outside, thus maintaining a high concentration gradient which promotes both convection and diffusion into the lens. For these reasons, horizontally-oriented lenses (high $r_{hv}$) are expected to have a lower salinisation rate than vertically-oriented lenses (low $r_{hv}$). This is corroborated by the fact that the values of $SP_{lo}$

after 12 and 40 d (Figs. 9e,f) are lower for configuration H than for configuration V.

The reasoning above holds only when the vertical-upward components develop, i.e., when $K_h/K_l < 100$ in these simulations. For the simulations that had $K_h/K_l > 100$ salinisation of the lenses is predominantly via diffusion. Also in this case there are clear differences in the salinisation rates of the lenses as reflected by the differences in $SP_{lo}$ after 12 and 40 d (Figs. 9e,f). Configuration B has the highest $SP_{lo}$ values and thus had the highest rates of lens salinisation (Fig. 9f). This is because the contact surface area between the lens and the high-permeability zone of this configuration is higher than for the two other configurations. The diffusion of salts into the lenses thus occurs over the highest surface area which explains the relatively-rapid increase of the solute mass within the lenses. The increase of solute mass within the lenses is lowest for configuration H. This is attributed to the entrapment of freshwater in the high-permeability zone below the lenses. Consequently, less saltwater is in contact with the lenses and the diffusive flux of salts remains relatively low. This latter observation means that the orientation of the lenses is also controlling salinisation of
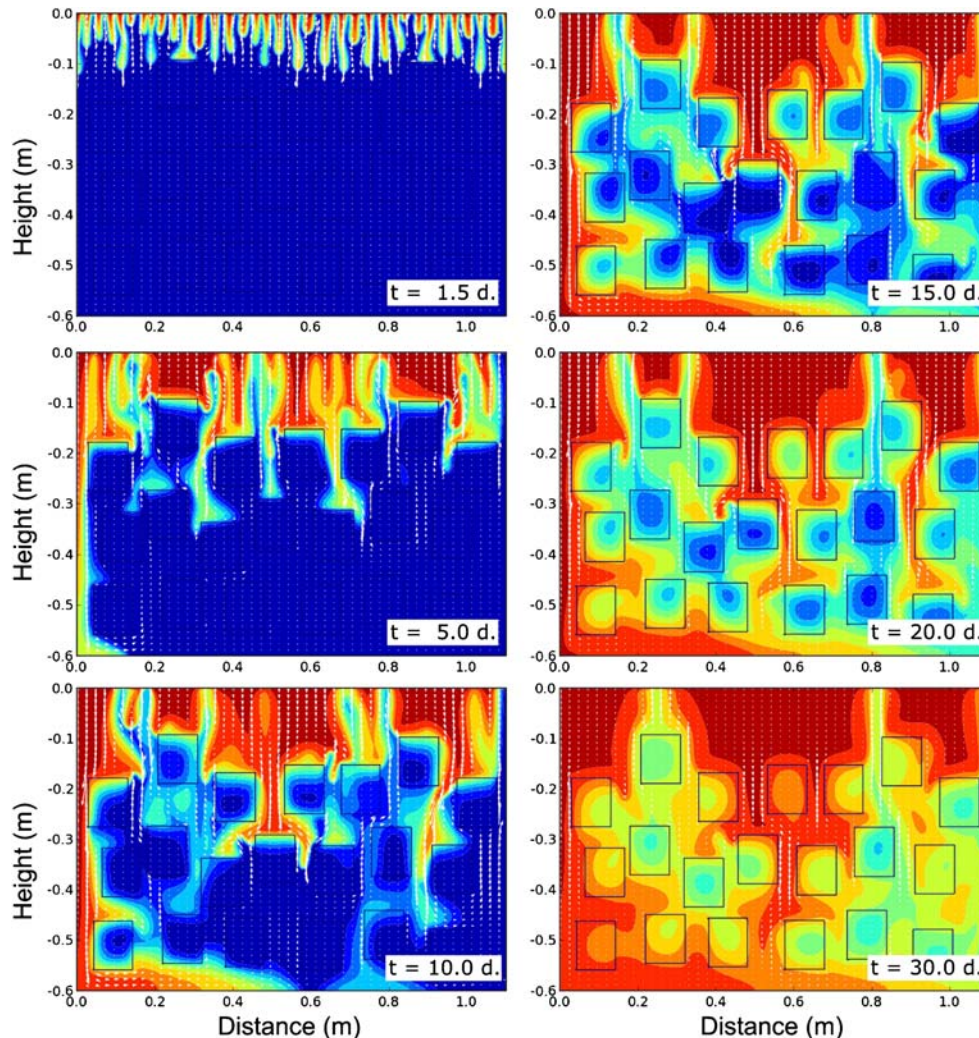
**Fig. 8** The development of salt fingers and flow vectors within the low-permeability lenses with time for simulation B$_{90}$. Results are shown for 1.5, 5, 10, 15, 20 and 30 d since the beginning of the simulation. Only the vector in every tenth column or layer is drawn

the low-permeability regions via their influence on the salinity distribution in the high-permeability region.

## Summary and conclusions

Using laboratory and numerical experiments, this study examined the critical control that geologic heterogeneity plays in the free convective process and on salt sequestration into low-permeability strata. A laboratory experiment was firstly performed and the results were shown to be in excellent agreement with those obtained using a numerical model. This laboratory and numerical modelling comparison provided an excellent foundation upon which to generalise results. Additional numerical simulations were then performed using a variety of different geological heterogeneity structures and geometrical configurations.

Previous studies have not focussed on the effect that discrete low-permeability structures have on the free convection process at the scale of individual lenses. The

precise local scale solute transport mechanisms that affect solute exchange between the layers of lower and higher permeability have not been reported in the literature. The findings corroborate the results from previous work (e.g., Simmons et al. 2001; Prasad and Simmons 2003; Nield and Simmons 2007) that the geometrical distribution of heterogeneities is a crucial factor in the development of free convective instabilities. The outcomes presented here illustrate the key characteristics of the flow and solute concentration patterns that may develop in the presence of low- and high-permeability zones.

A particular aspect of the free convection process that was observed in the experiments was the development of two convective flow fields that operate at different spatial and temporal scales, which were termed interlayer and intralayer convection. Interlayer flow occurs in the high-permeability regions of the domain and is driven by the buoyancy forces due to spatial density-differences. Intra-layer flow occurs in the low-permeability lenses. This latter sublayer scale process is driven by both larger scale
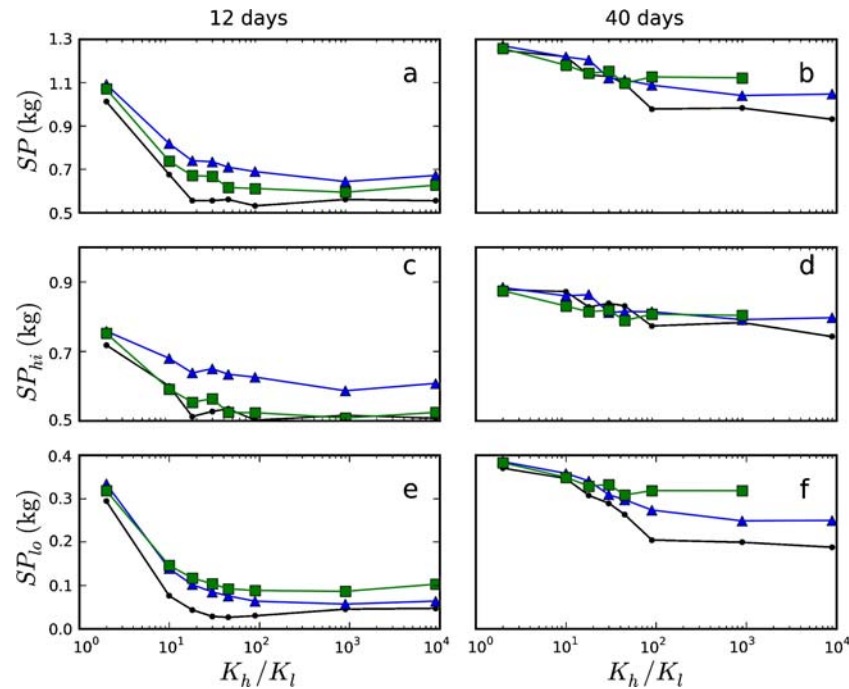
**Fig. 9** $SP$, $SP_{hi}$ and $SP_{lo}$ versus $K_h/K_l$ after 12 (*left panel*) and 40 d (*right panel*) since the start of the simulation. *Black*: configuration H, *blue*: configuration V, *green*: configuration B

interlayer convection and by the buoyancy of the freshwater within the low-permeability lenses.

The permeability of the lenses determines the strength of the intralayer flow components. If the permeability of the lenses increases and $K_h/K_l$ approaches unity, salinisation of the lenses becomes dominated by convective fingering. Conversely, as the permeability of the lenses decreases the flow within them becomes so weak that the sequestration of salts into the lenses is negligibly affected and diffusion is the prime mechanism of lens salinisation. In the experiments conducted during this study the transition between convective and diffusive salinisation of the low-permeability lenses occurred when $K_h/K_l > \sim 100$. This transitional behaviour has not been quantified in earlier work. Further work is needed to test the general applicability of and controls on the value of this apparent critical permeability contrast found in this study.

It was found that for $40 < K_h/K_l < \sim 100$, the interplay of inter- and intralayer flow is a critical factor in the sequestration of salts into the low-permeability structures. Interlayer processes such as entrapment of freshwater below and upward freshwater movement directly alongside lenses delay the build-up of salt mass within low-permeability regions. Upward, intralayer vertical flow initially retards salinisation of the lenses as these buoyant freshwater displacements oppose the downward penetration of dissolved salts by diffusion and free convection from above. Due to the presence of vertical upward flow, salinisation of the low-permeability structures eventually takes place from below, but at significantly later times, as saltwater is dragged upwards, i.e., salinisation occurs from below the low-permeability lens, not from above as may

have been intuitively expected. This is an unexpected outcome since the salt source is located above the low-permeability lenses. This bottom up convective salinisation process has not been described in previous literature.

The range of permeability contrasts over which the importance of intralayer flow effects were observed, is well within the range of conductivity ratios for geologic units that are usually considered to be homogeneous aquifers (Sudicky 1986). This implies that the use of an average permeability value for what may appear to be a weakly heterogeneous unit will incorrectly predict the macroscopic rate of salinisation by free convective fingering.

For the parameters used in the present numerical experiments, extensive salinisation of the lenses did not occur until after several days. Higher density contrasts, such as the one used in the tank experiment, may lead to increases of solute concentrations in the low-permeability regions after some hours. This timescale is a complicated function of factors such as the permeability contrast, lens geometry and fluid density and therefore the results presented here are not easily generalised.

A rather severe restriction of the present numerical study was the spatial extent of the domain, which was constrained by the extremely high computational burden of the simulations. Although it can be argued that the boundaries of the model domain represent natural hydrological features such as impermeable strata and flowlines, it would be desirable to examine these free convective and sequestration processes at field based spatial and temporal scales and contextualised within more specific hydrogeologic applications. At present, however, such simulations appear to pose computational challenges.

# References

Bachmat Y, Elrick DE (1970) Hydrodynamic instability of miscible fluids in a vertical porous column. Water Resour Res 6:156–171

Eggenkamp HGM, Middelburg JJ, Kreulen R (1994) Preferential diffusion of $^{35}$Cl relative to $^{37}$Cl in sediments of Kau Bay, Halmahera, Indonesia. Chem Geol 116:317–325

Elder JW (1968) The unstable thermal interface. J Fluid Mech 32:69–96

Groen J, Velstra J, Meesters AGCA (2000) Salinization processes in paleowaters in coastal sediments of Suriname: evidence from $\delta^{37}$Cl analysis and diffusion modelling. J Hydrol 234:1–20

Herweijer JC (1997) Sedimentary heterogeneity and flow towards a well. PhD Thesis, Vrije Universiteit Amsterdam, The Netherlands

Illangasekare T, Tyler SW, Clement TP, Villholth KG, Perera APGRL, Obeysekera J, Gunatilaka A, Panabokke CR, Hyndman DW, Cunningham KJ, Kaluarachchi JJ, Yeh WWG, van Genuchten MT, Jensen K (2006) Impacts of the 2004 tsunami on groundwater resources in Sri Lanka. Water Resour Res 42, W05201. doi:10.1029/2006WR004876

Kooi H, Groen J, Leijnse A (2000) Modes of seawater intrusion during transgressions. Water Resour Res 36:3581–3589

Langevin CD, Guo W (2006) MODFLOW/MT3DMS-based simulation of variable-density ground water flow and transport. Ground Water 44:339–351

Liu HH, Dane JH (1996) A criterion for gravitational instability in miscible dense plumes. J Contam Hydrol 23:233–243

Nield DA, Simmons CT (2007) A discussion on the effect of heterogeneity on the onset of convection in a porous medium. Transp Porous Med 68(3):413–421. doi:10.1007/s11242-006-9045-8

Nield DA, Simmons CT, Kuznetsov AV, Ward JD (2008) On the evolution of salt lakes: episodic convection beneath an evaporating salt lake. Water Resour Res 44, W02439. doi:10.1029/2007WR006161

Post VEA, Kooi H (2005) Rates of salinization by free convection in high-permeability sediments: insights from numerical modeling and application to the Dutch coastal area. Hydrogeol J 11(5) 549–559. doi:10.1007/s10040-003-0271-7

Prasad A, Simmons CT (2003) Unstable density-driven flow in heterogeneous porous media:A stochastic study of the Elder [1967b] "short heater" problem. Water Resour Res 39(1):1007–1028. doi:10.1029/2002WR001290

Riaz A, Hesse M, Tchelepi HA, Orr FM Jr (2006) Onset of convection in a gravitationally unstable diffusive boundary layer in porous media. J Fluid Mech 508:87–111. doi:10.1017/S0022112005007494

Schincariol RA, Schwartz FW (1990) An experimental investigation of variable density flow and mixing in homogeneous and heterogeneous media. Water Resour Res 26:2317–2329

Schincariol RA, Schwartz FW, Mendoza CA (1994) On the generation of instabilities in variable density flow. Water Resour Res 30:913–927

Schincariol RA, Schwarz FW, Mendoza CA (1997) Instabilities in variable density flows: stability and sensitivity analyses for homogeneous and heterogeneous media. Water Resour Res 33:31–41

Simmons CT (2005) Variable density groundwater flow: from current challenges to future possibilities. Hydrogeol J 13:116–119

Simmons CT, Narayan KA, Wooding RA (1999) On a test case for density-dependent groundwater flow and solute transport models: the salt lake problem. Water Resour Res 35:3607–3620

Simmons CT, Fenstemaker TR, Sharp JM (2001) Variable-density flow and solute transport in heterogeneous porous media: approaches, resolutions and future challenges. J Contam Hydrol 52:245–275

Simmons CT, Pierini ML, Hutson JL (2002) Laboratory investigation of variable-density flow and solute transport in unsaturated-saturated porous media. Transp Porous Med 47:215–244

Simmons CT, Sharp JM Jr, Nield DA (2008) Modes of free convection in fractured low-permeability media. Water Resour Res 44,W03431. doi:10.1029/2007WR006551

Sudicky EA (1986) A natural gradient experiment on solute transport in a sand aquifer: spatial variability of hydraulic conductivity and its role in the dispersion process. Water Resour Res 22:2069–2082

Volker A, Van der Molen WH (1991) The influence of groundwater currents on diffusion processes in a lake bottom: an old report reviewed. J Hydrol 126:159–169

Wooding RA (1962) The stability of an interface between miscible fluids in a porous medium. Zeitschr Angew Math Phys 13:255–266

Wooding RA (1969) Growth of fingers at an unstable diffusing interface in a porous medium or Hele-Shaw cell. J Fluid Mech 39:477–495

Wooding RA, Tyler SW, White I (1997a) Convection in groundwater below an evaporating salt lake: 1. onset of instability. Water Resour Res 33:1199–1217

Wooding RA, Tyler SW, White I, Anderson PA (1997b) Convection in groundwater below an evaporating salt lake: 2. evolution of fingers or plumes. Water Resour Res 33:1219–1228

Yamaguchi T, Sakamoto Y, Nakayama S, Vandergraaf TT (1997) Effective diffusivity of the uranyl ion in a granite from Inada, Ibaraki, Japan. J Contam Hydrol 26:109–117